



# Seasonal surface melt onset and firn freeze-up across the central Wrangell and St. Elias Mountains

Ingalise Kindstedt<sup>1,2</sup>, Andrew Johnson<sup>3</sup>, Kristin M. Schild<sup>1,2</sup>, Luke Copland<sup>4</sup>, Christine Dow<sup>5</sup>, Alison Criscitiello<sup>6</sup>, Dominic Winski<sup>1,2</sup>, Karl Kreutz<sup>1,2</sup>, and Seth Campbell<sup>1,2</sup>

<sup>1</sup>Climate Change Institute, University of Maine, Orono, Maine, USA

<sup>2</sup>School of Earth and Climate Sciences, University of Maine, Orono, Maine, USA

<sup>3</sup>Geophysical Institute, University of Alaska Fairbanks, Fairbanks, Alaska, USA

<sup>4</sup>Department of Geography, Environment and Geomatics, University of Ottawa, Ottawa, Ontario, Canada

<sup>5</sup>Department of Geography and Environmental Management, University of Waterloo, Ontario, Canada

<sup>6</sup>Department of Earth and Atmospheric Sciences, University of Alberta, Edmonton, Alberta, Canada

**Correspondence:** Ingalise Kindstedt (ingalise.kindstedt@maine.edu)

## Abstract.

High-elevation alpine firn is increasingly influenced by surface melt and meltwater retention, yet the spatial extent and timing of these processes remain poorly quantified. Here we present spatially distributed estimates of seasonal surface melt onset and firn freeze-up across the central Wrangell and St. Elias Mountains using time series C-band Synthetic Aperture Radar data from the Sentinel-1 mission, 2015–2024. Melt onset and freeze-up are identified from characteristic changes in backscatter associated with the presence of liquid water in snow and firn. Seasonal melt is detected across nearly all elevations in the range. Melt onset broadly tracks the seasonal rise of the 0°C isotherm up to ~3,000 m a.s.l., while freeze-up shows pronounced delays relative to subfreezing air temperatures at mid-elevations, indicating widespread meltwater retention within the firn. Combining freeze-up timing, air temperature, and elevation, we classify firn water-retention regimes and find that dry firn is confined to the highest elevations, covering only 3% of our area of interest. These results highlight the influence of meltwater on firn evolution in the Wrangell/St. Elias Mountains and demonstrate the utility of SAR for monitoring alpine glacier melt dynamics in data-sparse regions.

## 1 Introduction

Firn — snow that has survived at least one melt season — represents an intermediate stage in the transformation of new snow into glacial ice on glaciers and ice sheets worldwide (Miller, 1952). A healthy firn pack is essential for maintaining glacier mass balance; however, increasing evidence indicates that firn is warming and melting across many glacierized regions (Bezeau et al., 2013; Polashenski et al., 2014; Vandecrux et al., 2020; Ochwat et al., 2021; Horlings et al., 2022; Kindstedt et al., 2025).

Firn warming can modify its physical structure, thermal regime, and chemistry, thereby altering the thermal and chemical characteristics of developing glacier ice and compromising the climate records archived within (Samimi and Marshall, 2017; Ochwat et al., 2021; Kindstedt et al., 2025). In addition, porous firn can act as a buffer to glacier runoff, delaying the transfer of meltwater to downstream hydrological systems by years to decades in some regions (Harper et al., 2012; Koenig et al., 2014;



MacFerrin et al., 2019; Culberg et al., 2021). When surface meltwater is retained within the firn pack as a firn aquifer, it may be stored for several years, further warming the firn while delaying runoff (Fountain, 1989; Schneider, 1999; Jansson et al., 2003; Miège et al., 2016; Ochwat et al., 2021). Conversely, near-surface refreezing of meltwater into ice layers can reduce firn permeability and increase runoff over longer timescales (Machguth et al., 2016; MacFerrin et al., 2019). The presence of liquid water within snow and firn can also inhibit drilling access to underlying ice, complicating the recovery of preserved climate records. In short, crossing the cold-to-temperate firn threshold shifts firn evolution from dry densification to meltwater-driven processes, fundamentally altering glacier ice development, hydrologic buffering, and the preservation and recovery of climate records.

Net firn warming over the course of a year occurs when the energy transferred into the firn during the melt season exceeds the regeneration of cold content during the winter, with cold content referring to the amount of energy required to raise the temperature of a given volume of firn to 0°C (Vandecrux et al., 2020). When the snow surface is warmer than the firn column beneath (e.g. during the summer melt season), energy is transferred to the subsurface via conduction and meltwater percolation. In particular, the release of latent heat associated with subsurface refreezing of meltwater is a dominant factor in downward heat transport through snow and firn (Cuffey and Paterson, 2010).

While surface energy balance modeling provides the most complete framework for quantifying heat transfer and melt processes, its application at regional scales is often limited by the availability of distributed meteorological forcing and surface property data. Consequently, air temperature is often used as a first-order proxy for melt occurrence in glacierized regions (Hock, 2003). However, air temperature alone provides an incomplete proxy for firn thermal evolution, as it does not capture the spatial and temporal variability of meltwater production, percolation, and refreezing that dominate firn heat transfer. Whether firn remains cold or transitions toward temperate conditions depends not only on melt season surface temperature, but also on the subsurface retention of liquid water into the fall and winter, which, through latent heat release, reduces the efficiency of wintertime cold content regeneration.

The Wrangell and St. Elias Mountains (henceforth “Wrangell/St. Elias”) are adjacent heavily glacierized mountain ranges located on the border of Alaska and southwest Yukon (Fig. 1). High annual snow accumulation that insulates underlying firn (Marcus and Ragle, 1970), together with amplified high-elevation warming (Williamson et al., 2020) make Wrangell/St. Elias susceptible to increasing firn meltwater retention and aquifer development. Recent observations from field sites around 2,600 m a.s.l. to 3,000 m a.s.l. on the northeast side of Wrangell/St. Elias have shown evidence of firn warming and increased surface melt production and percolation (Ochwat et al., 2021; Kindstedt et al., 2025). However, to date, no comprehensive survey of surface melting across the range has been undertaken.

Here we use satellite Sentinel-1 Synthetic Aperture Radar (SAR) data to derive spatially distributed surface melt onset and firn freeze-up dates, independent of air temperature, for each year from 2015–2024 across the central Wrangell/St. Elias, and apply a novel approach for the identification of firn melt zones. Our results highlight the spatial variability in melt season timing and reveal widespread firn meltwater retention across the region.



55 2 Methods

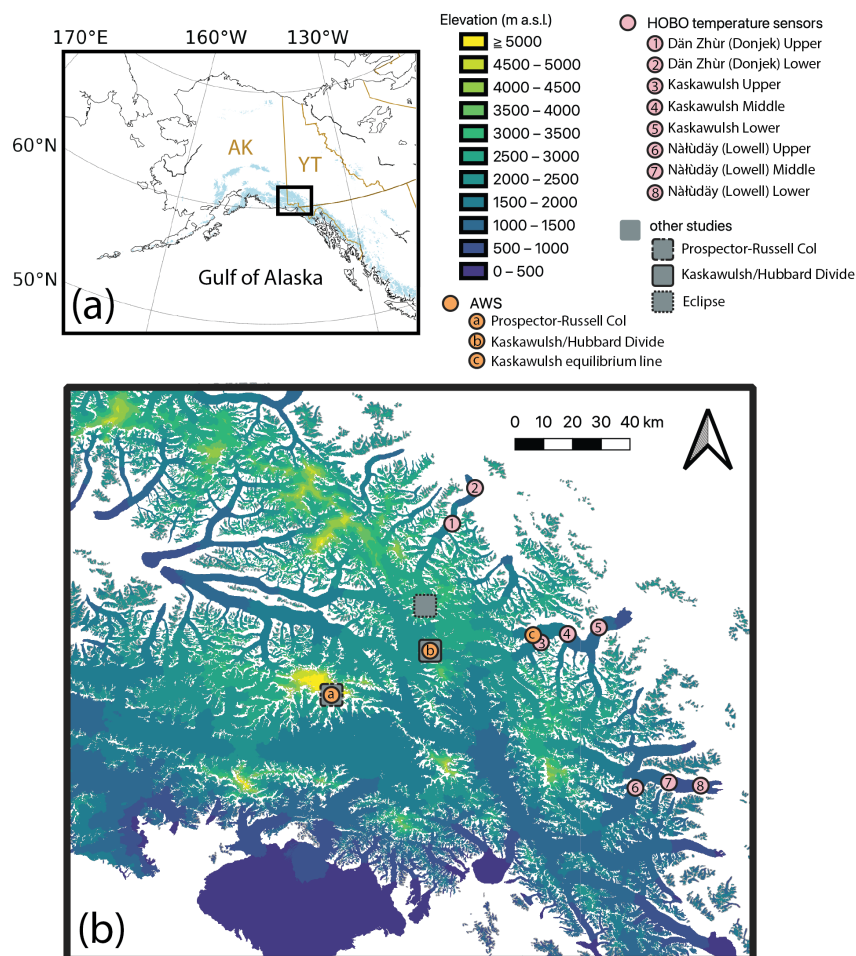


**Figure 1.** Study area of interest (AOI) across Alaska (AK) and Yukon (YT) with digital elevation map (DEM) and ground-truth sites. A regional overview map is shown in panel (a) with the AOI extent indicated by the black rectangle. Binned elevations and ground-truth sites (colored circles and gray squares) across the AOI are shown in panel (b).

**2.1 Region of Study**

We focus our analyses on the central Wrangell/St. Elias Mountains, and define our area of interest (AOI) as the area from 59.7586° N to 61.4825° N and 137.8171° W to 142.0295° W (45,470 km<sup>2</sup>, 0–5,959 m a.s.l., Fig. 1). Rising over 5,000 m from sea level within 100 km of the coast, Wrangell/St. Elias represents one of the most dramatic barriers to inland transport of coastal moisture on the planet (Newman et al., 2020). Orographic precipitation resulting from this topography (mean 0.59 m



w.e.  $a^{-1}$  at the Kaskawulsh/Hubbard Divide; Fig. 1; Kindstedt et al., 2026) sustains the extensive glaciers and icefields found in the range. We define our AOI to include the most heavily glaciated central Wrangell/St. Elias, characterized by interconnected glaciers and broad icefields rather than isolated small alpine glaciers. Fifty-one percent (23,190 km<sup>2</sup>) of the land surface area in our AOI is ice-covered, and feeds two of the largest watersheds (by discharge) that drain into the Gulf of Alaska: the Copper and the Alsek Rivers (Sergeant et al., 2020). The remainder of the land surface within our AOI is a mix of ocean, coastal plain, interior forest, waterways, and steep rocky slopes.

## 2.2 Sentinel-1 Synthetic Aperture Radar (SAR) satellite imagery

To identify the onset and extent of surface melt in Wrangell/St. Elias, we utilize the dramatic drop in C-band SAR backscatter associated with the introduction of liquid water to a snowpack (Nagler and Rott, 2000; Nagler et al., 2016; Tsai et al., 2019). C-band SAR is an active microwave remote sensing technique that transmits radar pulses and measures the energy scattered back from the surface, making it sensitive to snow structure and dielectric properties. C-Band SAR is able to operate at night and through cloud cover, and is very strongly attenuated by water, providing a clear signal of melt onset despite dark or overcast conditions. In particular, we use backscatter measured by the Sentinel-1 (S1) mission in the interferometric wide beam mode because of its ability to produce imagery at sub-weekly temporal resolution (6-day revisit time) and high spatial resolution (20 m) across a 250 km wide swath. In addition, the operational wavelengths (centered at 5.56 cm) of Sentinel-1 are two orders of magnitude larger than typical snow grain sizes (0.1-0.3 mm; Tsai et al., 2019). Therefore, although grain size can affect SAR backscatter, it has a negligible influence on Sentinel-1 data. We use S1 scenes in VV polarization because it is more sensitive to surface conditions, whereas VH polarization is more strongly influenced by volume scattering within the snowpack (Lievens et al., 2019).

Because the magnitude of backscatter return varies with the satellite angle of incidence, the look geometry of all scenes in a single SAR timeseries must remain consistent. We therefore treat scenes from each path/frame as independent timeseries and then merge the independent sets of results by selecting the earliest identified melt onset and freeze-up dates from all path/frames for each pixel where overlap occurs. Additionally, we only use path/frames where scenes are acquired before 10:00 local time (all scenes in our AOI are acquired either before 10:00 or after 18:00) to eliminate biased earlier melt detection for pixels with afternoon image acquisitions. Sentinel-1 path/frames and scenes used in this study are provided in Appendix A.

Our analysis spans the 2015–2024 melt seasons, beginning with the launch of the first Sentinel satellite (Sentinel-1a, S1A) in 2014 (12-day revisit) and then including the addition of Sentinel-1b (S1B) data from 2017 through 2022 (resulting in a 6-day revisit time). Gaps in available S1 data temporarily reduce the temporal resolution of our timeseries and are addressed within our uncertainty calculations below (Section 2.3).

## 2.3 Melt classification

The SAR-based melt detection method we use relies on the contrast between dry snow and melting snow backscatter values. Following Scher et al. (2021) and Nagler and Rott (2000), we use a timeseries of backscatter values from each pixel to classify that pixel as either dry or melting at the time of acquisition. A schematic of our melt classification method is shown in Figure



2. Because melt is identified individually for each pixel relative to its dry-snow backscatter value, we first produce a reference  
95 dry-snow image from at least four wintertime (Nov-Mar) scenes. Pixels are then classified as melting when their backscatter  
value is  $>3$  dB lower than their dry-snow average; otherwise, pixels are classified as dry. To establish melt onset each year,  
we identify the first of at least two consecutive melting scenes in each pixel's backscatter timeseries and set melt as the date  
of image acquisition. We consider the uncertainty in melt onset date to be the number of days passed since the last dry S1  
100 observation before onset. We exclude pixels where melt onset is identified to be later than day 244 (September 1 in non-leap  
years).

We identify freeze-up, or refreezing of the snow and firn, as the first of at least two consecutive dry scenes following  
a period of seasonal melting. The penetration depth of C-band SAR in wet snow (e.g. during the summer melt season) is  
only a few centimeters; however, as the snow and firn refreeze, Sentinel-1 can penetrate meters to tens of meters (Baghdadi  
et al., 1997; Tsai et al., 2019). Freeze-up timing inferred from increases in SAR backscatter may therefore reflect multiple  
105 processes, including surface refreezing, drainage, and firn structural change. As such, we use the term freeze-up to represent  
an integrated firn column response to changes in structure and liquid water content rather than a discrete physical threshold in  
surface conditions. We define the uncertainty in freeze-up date as the number of days elapsed since the last melting Sentinel-1  
observation prior to freeze-up. We exclude pixels where freeze-up is identified earlier than day 244. When averaging melt onset  
or freeze-up date over multiple years, we consider the associated uncertainty (in days) to be the maximum uncertainty value  
110 among the individual years averaged.

## 2.4 Image processing

We access and pre-process Sentinel-1 images through the Alaska Satellite Facility (ASF) to produce radiometrically terrain  
corrected images using ASF's Hybrid Pluggable Processing Pipeline (HyP3) with the Copernicus DEM at 30 m resolution  
(Hogenson et al., 2020). During pre-processing, we identify path/frames that intersect our area of interest, and remove those  
115 with fewer than four wintertime (Nov-Mar) scenes or without scenes after March 31. We then reproject the images and convert  
backscatter values to decibels (dB; Fig. 2). To reduce speckling in our results, we apply a median filter with a kernel size  
of 5 to each scene in the dry-snow winter average and in the melt season timeseries. We isolate low-angle ( $<30^\circ$ ) glacier  
slopes, as steeper slopes tend to have chaotic and changing ice surfaces that are not conducive to SAR timeseries analysis (Shi  
and Dozier, 1995), using a mask based on the Randolph Glacier Inventory Version 7.0 (RGI 7.0 Consortium, 2023) and the  
120 Copernicus DEM (European Space Agency (ESA), 2014). Pixels where the standard deviation of winter backscatter values  
is  $>3$  dB (the established melt detection threshold) are excluded from analysis because a 3 dB drop in backscatter is not  
physically meaningful in these areas. The implementation code we build from can be found on Github (Johnson, 2023).

## 2.5 Geography and terrain

The SAR-based melt detection method relies on isolating the contrast between dry snow and melting snow backscatter values,  
125 which is most reliable in the accumulation zone, where surface conditions are more consistent than in the ablation zone.  
However, this requires some prior knowledge of where the equilibrium line altitude (ELA) is, a feature which is itself difficult

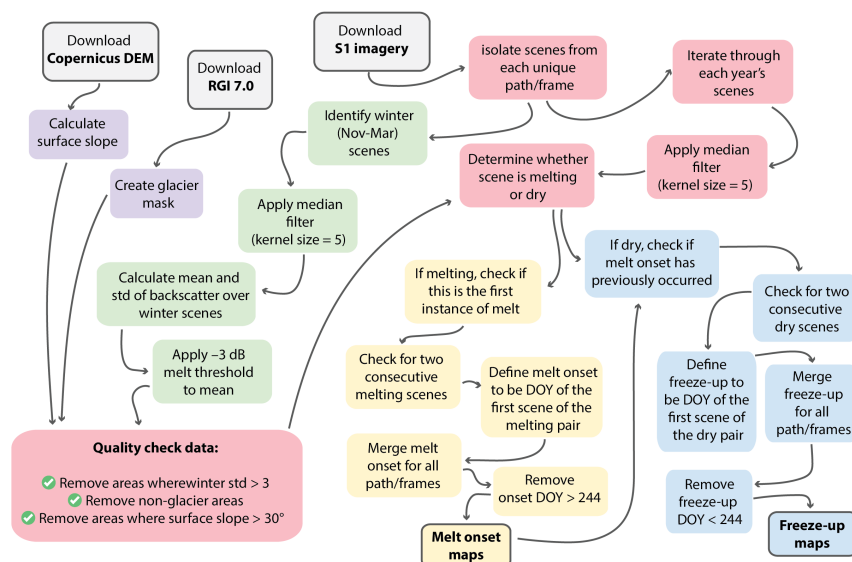


**Figure 2.** Schematic of processing Sentinel-1 imagery to derive melt onset date. Gray boxes indicate initial files downloaded. Purple boxes indicate preparatory steps. Green boxes describe the generation of a reference winter dry-snow image. Pink boxes describe the iteration over images in each melt season timeseries, including the execution of a quality check. Yellow boxes describe the determination of melt onset for each pixel. Blue boxes describe the determination of freeze-up for each pixel.

to identify. We therefore do not apply any elevation- or zone-based filters, instead taking local context into account during interpretation of our results. To investigate the effect of terrain features on melt onset and freeze-up data, we implement a Random Forest algorithm with 200 decision trees to quantify the amount of variability in onset and freeze-up that can be explained by elevation, distance from the ocean, slope angle, and aspect (separated into ‘northness’ and ‘eastness’).

## 2.6 Air temperatures

We compare our SAR-based melt detection with air temperature measurements from shielded automatic weather stations (AWS) and HOBO temperature loggers (Table 1) to ground-truth our melt detection and evaluate how well air temperature at the surface represents subsurface firn conditions. To do this, we compare our melt onset and freeze-up results to (1) positive degree days calculated from air temperatures, and (2) the seasonal migration of the 0°C isotherm. To track the 0°C isotherm, we first calculate daily regional lapse rates from 0 to 6,000 m a.s.l. using temperature data from three HOBO sensors (Kaskawulsh Lower, Kaskawulsh Middle, Kaskawulsh Upper) and two AWS (Kaskawulsh/Hubbard Divide and Prospector-Russell Col). We use the Kaskawulsh Upper HOBO data rather than the nearby (within 100 m elevation) Kaskawulsh ELA AWS data because the HOBO sensor is located on glacier ice while the AWS is located on a bedrock nunatak, and the HOBO sensor provides more recent data (Table 1). We select the series of stations going from the lower Kaskawulsh Glacier to Prospector-Russel



Col for its spatial coverage over nearly the entirety of the elevation range within our AOI, and because its temporal coverage began nearly two years earlier than measurements on the nearby Dän Zhùr Glacier (Fig. 1). We then perform a least squares linear regression on overlapping mean daily temperature values from all five selected stations (August 2017 – February 2023). Finally, we use the resultant daily lapse rates to compute isotherms at 2°C intervals from -20°C to 20°C for comparison with our melt onset and freeze-up results. A comparison of isotherms computed from Kaskawulsh vs. Dän Zhùr data over their period of overlap (July 2019 – February 2023) is provided in Appendix B.

**Table 1.** Ground-truth data used in this study. Locations of all stations are shown in Fig. 1

Station name	Lat/Lon	Elevation (m a.s.l.)	Time period covered
Prospector-Russel (PR) Col AWS	60.5670° N, 140.4053° W	5,640	2021–2023
Kaskawulsh/Hubbard Divide AWS	60.7003° N, 139.7999° W	2,603	2015–2023
Kaskawulsh equilibrium line AWS	60.7421° N, 139.1659° W	1,800	2019–2023
Dän Zhùr (Donjek) Upper HOBO	61.0800° N, 139.6644° W	1,674	2019–2025
Dän Zhùr (Donjek) Lower HOBO	61.1858° N, 139.5242° W	1,241	2019–2025
Kaskawulsh Upper HOBO	60.7299° N, 139.1253° W	1,709	2018–2025
Kaskawulsh Middle HOBO	60.7507° N, 138.9628° W	1,503	2017–2023
Kaskawulsh Lower HOBO	60.7704° N, 138.7633° W	1,192	2018–2025
Nàfùdäy (Lowell) Upper HOBO	60.2853° N, 138.5393° W	1,268	2017–2025
Nàfùdäy (Lowell) Middle HOBO	60.3018° N, 138.3335° W	1,041	2012–2022
Nàfùdäy (Lowell) Lower HOBO	60.2921° N, 138.1382° W	776	2017–2022

## 2.7 Firn zone classification

To enable assessment of the spatial distribution of firn water-retention regimes, we combine Sentinel-derived freeze-up dates, in situ air temperatures, and elevation data to classify pixels into one of five SAR-based firn melt zones:

1. **Dry firn:** accumulation zone with little to no retention of liquid water in the firn
2. **Dry to wet firn:** zone where pixels transition from dry to wet firn with decreasing elevation
3. **Wet firn:** accumulation zone with extensive melt percolation and retention in the firn
4. **Wet firn to ablation zone:** zone where pixels transition from wet firn to ablation zone with decreasing elevation
5. **Ablation zone:** zone with no retention of snow or firn from one winter to the next

These zones are intended to capture differences in liquid water retention and melt influence as expressed in SAR backscatter behavior, not to map directly onto classically defined glacier melt facies. We perform firn-zone classification on a per-pixel basis restricted to glacierized areas using our RGI 7.0 glacier mask (RGI 7.0 Consortium, 2023). The resulting firn-zone



map delineates spatially coherent firn water-retention regimes inferred from the combined influence of elevation and seasonal refreeze timing, rather than direct observations of firn stratigraphy.

160 We define our firn zones based on the behavior of freeze-up detected in the S1 SAR data relative to the annual onset of subfreezing air temperatures ( $\Delta freeze$ ). In areas where liquid water is retained within the firn, the return to winter dry-snow backscatter values is delayed relative to the autumn onset of subfreezing air temperatures, reflecting the downward propagation of a freezing front that progressively increases backscatter as deeper firn layers refreeze (Rau et al., 2000; Winsvold et al., 2018; Scher et al., 2021). In particular, we compute the average  $\Delta freeze$  over 100-m elevation bins, and then assign each  
165 DEM pixel the  $\Delta freeze$  value corresponding to its bin. A greater  $\Delta freeze$  indicates greater retention of liquid water.

Each of our five firn zones is either stable (dry firn, wet firn, ablation zone) or transitional (dry to wet firn, wet firn to ablation zone). Note that we use the term "transitional" here to describe a transition with elevation rather than with time. Before assigning each pixel to a specific firn zone, we use a novel technique to classify it as either stable or transitional based on the vertical gradients of  $\Delta freeze$  with elevation. Elevations with low vertical  $\Delta freeze$  gradients are stable, while those  
170 with high vertical  $\Delta freeze$  gradients are transitional (Fig. C1).

To calculate vertical  $\Delta freeze$  gradients, we first smooth  $\Delta freeze$  profiles using a Savitzky–Golay filter to suppress small-scale noise while preserving large-scale structure. Where insufficient data density preclude Savitzky–Golay filtering, we apply a centered rolling mean. We then compute the vertical gradient of the smoothed  $\Delta freeze$  profile to characterize the rate of change in seasonal backscatter response with elevation. We smooth the absolute value of this gradient over a vertical window  
175 of 150 m, and define transitional firn zones as continuous elevation bands where the smoothed absolute gradient exceeds the 75th percentile of its distribution. We exclude bands less than 200 m thick to avoid overdetection.

Our gradient-based stability classification results in two distinct transitional elevation ranges. We define our three stable firn zones based on their elevation relative to those two transitional ranges. Elevations below the lower transition zone are classified as ablation zone. Elevations between the two transition zones are classified as wet firn. Elevations above the upper transition  
180 zone are classified as dry firn.

## 2.8 Surface energy balance

The energy available for melt can be represented as the net energy balance at the glacier surface ( $E_N$ ; Cuffey and Paterson, 2010).  $E_N$  can be expressed as the sum of component energy fluxes, defined here as positive when they represent a flow of energy into the glacier surface:

$$185 \quad E_N = E_S + E_L + E_G + E_H + E_E + E_P \quad (1)$$

where  $E_S$  is the net shortwave radiation,  $E_L$  is the net longwave radiation,  $E_G$  is the subsurface energy flux,  $E_H$  and  $E_E$  are the turbulent sensible and latent heat fluxes, and  $E_P$  is the heat flux associated with liquid precipitation that subsequently freezes (Cuffey and Paterson, 2010). A positive  $E_N$  will drive melt if the surface has warmed to the melting point, whereas a negative  $E_N$  will drive freezing of any available liquid water (Cuffey and Paterson, 2010). Contributions to  $E_N$  tend to be



190 dominated by the radiative ( $E_S$  and  $E_L$ ) and turbulent ( $E_H$  and  $E_E$ ) fluxes (Hock, 2005; Cuffey and Paterson, 2010). Because both  $E_L$  and  $E_H$  increase with atmospheric temperature, atmospheric warming is a key driver of surface melt production; however, the magnitude of its effect on  $E_N$  varies over space and time (Cuffey and Paterson, 2010).

To compare the relative contributions of radiative and turbulent fluxes to the surface energy balance (SEB) across elevations, we apply the SEB model of Matthews et al. (2020), previously developed for a similar glacierized alpine environment in the Himalaya, to AWS data from three sites: Prospector-Russel Col (PR Col; 5,640 m a.s.l.), the Kaskawulsh/Hubbard Divide (K/H Divide; 2,603 m a.s.l.), and the Kaskawulsh ELA (1,800 m a.s.l.; Fig. 1; Table 1). Incoming shortwave radiation is measured directly at all three AWS sites and combined with a prescribed constant albedo of 0.8 (old, clean, dry snow; Cuffey and Paterson, 2010), applied uniformly across sites and time, to calculate  $E_S$ . Although snow surface albedo can vary widely (0.5–0.98; Cuffey and Paterson, 2010), higher elevations are generally characterized by dry, minimally metamorphosed snow and thus higher albedo. As a result, our estimates of the relative contribution of shortwave radiation to SEB at Prospector-Russel Col compared to the lower sites are likely conservative. Net longwave radiation is estimated using the Brutsaert (1975) clear-sky emissivity parameterization based on measured air temperature and relative humidity. Turbulent heat fluxes are calculated using the bulk aerodynamic method (Hock, 2005), with identical parameterizations applied at all sites. We run the model with 2-minute timesteps to resolve diurnal variability and then downsample output fluxes to daily means. Note that our SEB modeling is intended to be comparative rather than predictive; the assumptions listed above are consistent with this focus and do not affect the qualitative differences in SEB contributions observed across elevations.

### 3 Results

#### 3.1 Surface melt onset

We detect seasonal melting across virtually all elevations (up to 5,908 m a.s.l.) in the Wrangell/St. Elias Mountains. However, the percentage of melting pixels drops from >85% between 2,000 and 3,000 m a.s.l. to <15% between 4,000 and 5,000 m a.s.l. to only 1% of pixels above 5,000 m a.s.l. (Fig. 5d).

From 2018–2021 (years with >45% S1 coverage over the glacierized portion of our AOI), we find melt onset across much of Wrangell/St. Elias to occur on average between day of year (DOY) 125 and 175 (approximately May 5th to June 25th, Fig. 3). We find the timing of melt onset to generally coincide with the seasonal rise of positive degree days (PDDs) in the spring and summer, but do not identify any specific threshold in PDDs that corresponds to melt onset (Fig. 4). Melt onset and freeze-up maps for individual years 2015–2024 can be found in Appendix D.

Melt onset shows a positive relationship with elevation that closely tracks the upward migration of the 0°C isotherm until around 3,000 m a.s.l., providing a nice validation for SAR-based melt detection. Note, however, that the most consistent onset dates and strongest coherence with above-freezing air temperatures occur between 1,900 m a.s.l. and 3,000 m a.s.l. (Fig. 5). Above 3,000 m a.s.l., the 0°C isotherm no longer rises systematically, and melt onset occurs at similar DOY even as elevation increases (Fig. 5a). Although elevation is the dominant determinant of melt onset across our AOI, there is a dramatic reduction in its importance relative to other terrain characteristics above 3,000 m a.s.l. (Fig. 6). When considered together across the

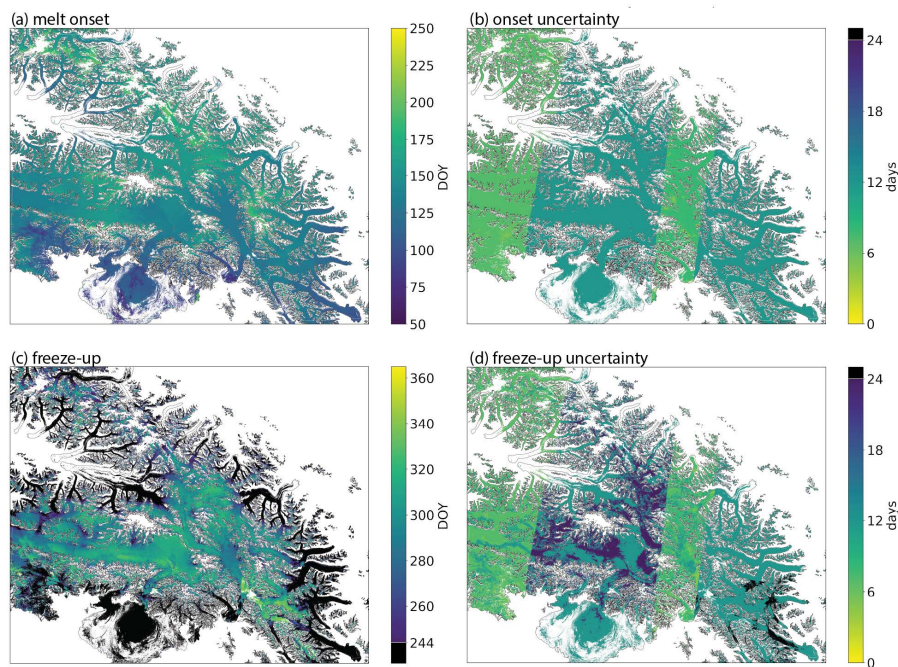


**Figure 3.** Spatial distribution of mean melt onset (a) and freeze-up (c) day of year (DOY) from 2018–2021, and the associated uncertainty in days (b,d).

entire AOI, elevation, distance from ocean, slope angle, and aspect explain 61% of variability in melt onset date, with an average prediction error of 12 days (random forest analysis).

### 225 3.2 Firn freeze-up

Freeze-up across much of Wrangell/St. Elias from 2018–2021 occurs on average between DOY 260 and 340 (approximately September 17th to December 6th, Fig. 3).

Freeze-up does not mirror the downward migration of the 0°C isotherm in the fall (Fig. 5). Freeze-up is most delayed relative to 0°C air temperatures between approximately 1,900 and 3,000 m a.s.l. ( $\Delta freeze > 100$  days). Above 3,300 m a.s.l.,  
230  $40 < \Delta freeze < 70$  days. Below 1,600 m a.s.l.,  $\Delta freeze < 50$  days.

When considered together across all elevations, our five terrain characteristics explain 25% of variability in freeze-up date, with an average prediction error of 24 days. Distance from ocean shows the greatest predictive capacity for freeze-up (negatively related) below 3,000 m a.s.l., while its importance is reduced relative to elevation and slope angle above 3,000 m a.s.l. (Fig. 6).

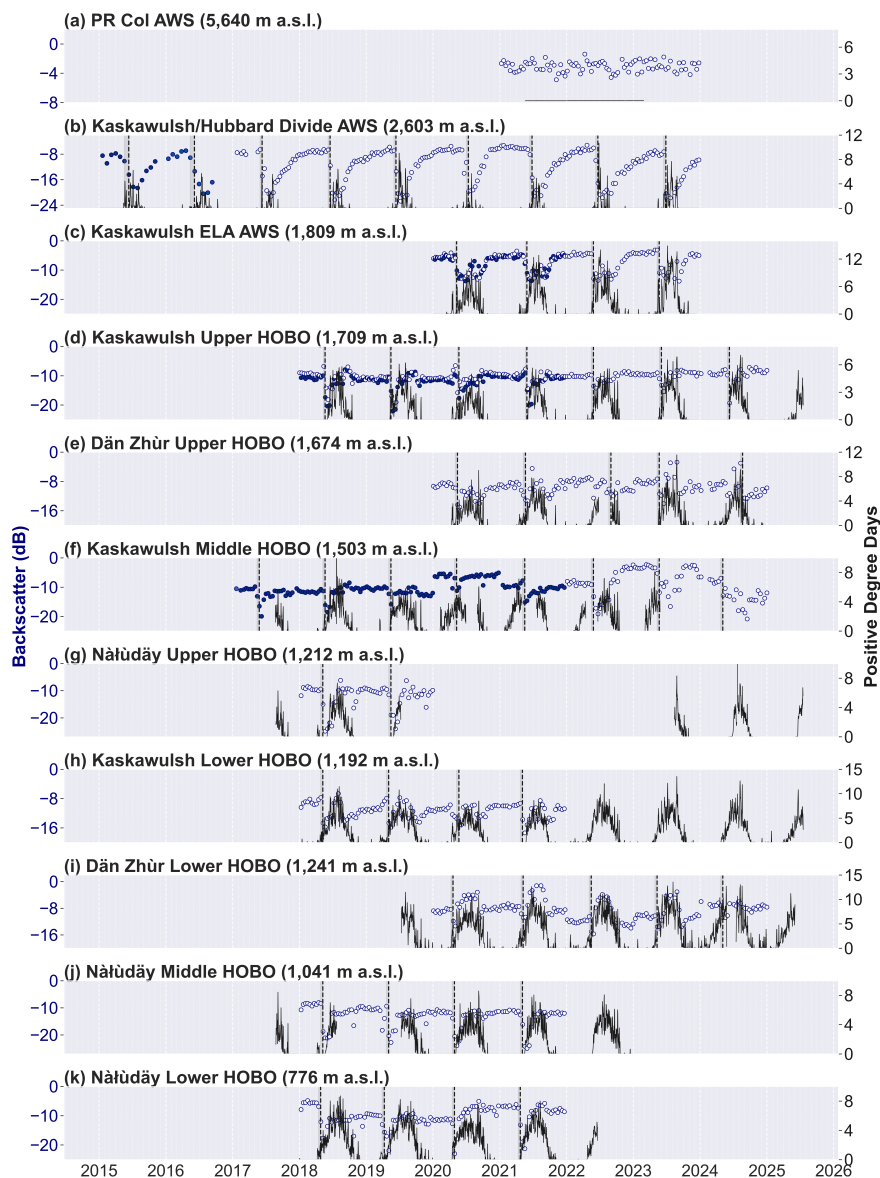


**Figure 4.** Sentinel-1 backscatter (blue circles) and positive degree days (PDDs, black line) at calculated from air temperatures at automated weather station (AWS, panels a-c) and HOBO temperature logger (panels d-k) sites. Sites are shown from highest to lowest elevation. For sites with two overlapping path/frames, the backscatter timeseries for one is shown with open circles, while the backscatter timeseries for the other is shown with filled circles. SAR-derived melt onset day of year (DOY) is shown by the vertical dashed line, with the associated uncertainty (days) shown by the gray bar. Note that HOBO sensors are located on glacial ice, while AWS are located on bedrock nunataks (Fig. 1).

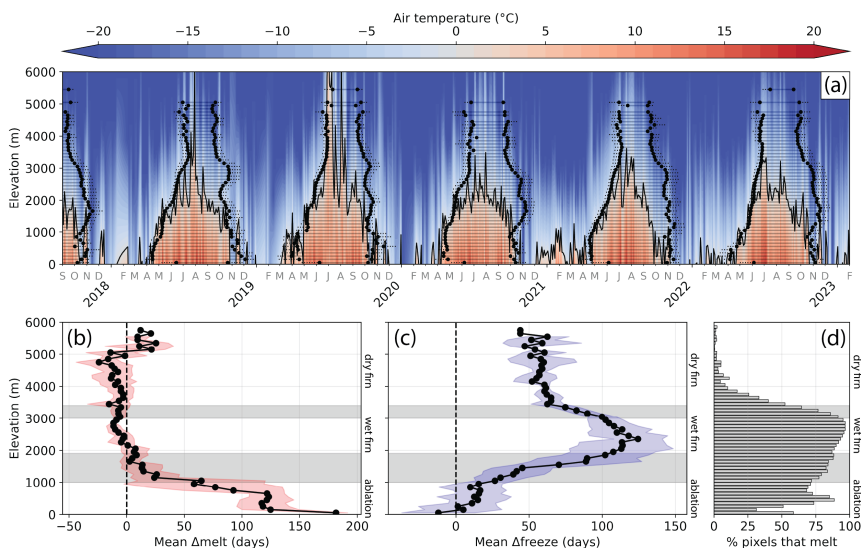


**Figure 5.** Mean melt onset and freeze-up relative to seasonal migration of the 0°C isotherm. Panel (a) shows melt onset and freeze-up dates (black solid circles) averaged over 100 m elevation bins plotted with spatially integrated air temperatures (colorbar). Air temperatures were estimated from lapse rates computed using data from five in situ stations ranging in elevation from 1,192–5,640 m a.s.l.. The black line represents the 0°C isotherm. Panel (b) shows the offset between Sentinel-1 melt onset and the DOY of 0°C air temperatures across elevation bands ( $\Delta_{melt}$ ). Panel (c) shows the offset between Sentinel-1 freeze-up and the DOY of 0°C air temperatures across elevation bands ( $\Delta_{freeze}$ ).  $\Delta_{melt}$  is averaged across 2018–2022.  $\Delta_{freeze}$  is averaged across 2017–2022. Standard deviations are shown by the shaded red (melt) and blue (freeze) envelopes. Panel (d) shows the percentage of pixels in each elevation band that melt. Our firn water-retention zones are shown by the horizontal shaded gray bands in panels (b-d).

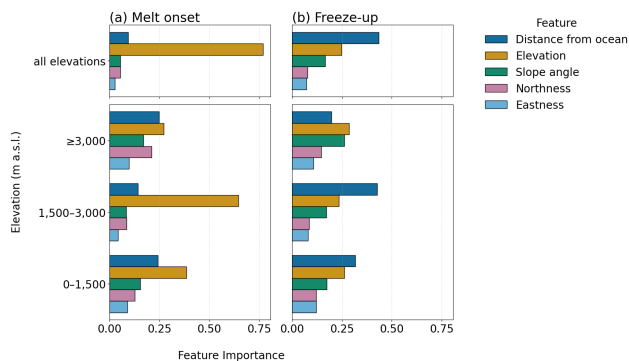


**Figure 6.** Relative importance of terrain features in determining melt onset (a) and freeze-up (b) dates. Relative importance over all elevations is shown in the top set of panels. Relative importance for pixels at low (0–1,500 m a.s.l.), middle (1,500–3,000 m a.s.l.) and high (above 3,000 m a.s.l.) elevations are shown in the bottom set of panels.

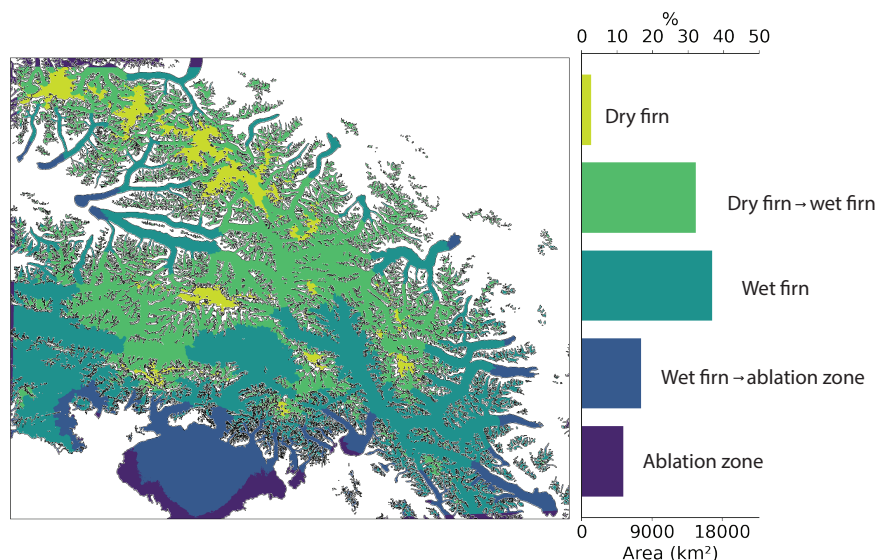


**Figure 7.** Firm-zone classification across the study area from 2018–2022 derived from Sentinel-1 freeze-up timing, air temperature, and elevation. Pixels are classified as dry firm, wet firm, ablation zone, or transitional regimes based on the vertical gradient in the delay in freeze-up relative to the onset of subfreezing air temperatures and elevation. The area and percentage of total pixels contained in each firm zone are shown in the righthand panel.

### 235 3.3 Firm zone classification

Based on the behavior of firm freeze-up across our AOI (Fig. C1), we find that 12% (5,318 km<sup>2</sup>) of our AOI is in the ablation zone, 36% (16,687 km<sup>2</sup>) is in the wet firm zone, and only 3% (1,174 km<sup>2</sup>) is in the dry firm zone (Fig. 7). The remaining 49% of our AOI is in a transition zone either from dry firm to wet firm (32%) or wet firm to ablation zone (17%). Wet firm and ablation zone areas are concentrated in the broad, low-elevation, coastal glaciers in the south of our AOI, while dry firm is concentrated around the high peaks mostly found in the central and northern areas of our AOI (Fig. 7).

### 3.4 Surface energy balance

Radiative heat fluxes are predominantly positive at the K/H Divide and the Kaskawulsh ELA, while turbulent fluxes are predominantly negative, aside from a summer interval of positive sensible heat flux. At PR Col, only net shortwave radiation is predominantly positive (Fig. 8).



**Figure 8.** Modeled components of the surface energy balance (SEB) at Prospector-Russel Col (a), the Kaskawulsh/Hubbard Divide (b), and the Kaskawulsh ELA (c). The net SEB is shown by a black line, while individual components are shown in the stacked line plot. The gray shaded area in panel (a) indicates the period of time when wind speed measurements used to calculate the sensible and latent heat fluxes were unavailable at PR Col. Because the analysis focuses on relative flux contributions using identical model parameterizations across sites, systematic uncertainties are expected to affect all sites similarly and are therefore not shown.

## 245 4 Discussion

### 4.1 Surface melting and energy balance

The relatively constant range of melt onset dates in Wrangell/St. Elias across elevations  $>3,000$  m a.s.l. compared to at lower elevations may reflect the outsize influence of incoming solar radiation relative to air temperatures in producing melt above  $>3,000$  m a.s.l. Generally, longwave radiation is a dominant component in surface energy balance and contributor to surface melting (Cuffey and Paterson, 2010), which is reflected in the correspondence between surface melt onset and the migration of the  $0^{\circ}\text{C}$  isotherm (Fig. 5). However, surface melting can be driven by shortwave radiation (insolation) even when air temperatures remain below  $0^{\circ}\text{C}$ , as they largely do at higher elevations in our AOI (Matthews et al., 2020; Scher et al., 2021). Notably, we detect surface melting in a small ( $<15\%$ ) but non-zero percentage of pixels above 4,000 m a.s.l. despite a near absence of above-freezing temperatures.

255 Our SEB modeling indeed indicates that net shortwave radiation is the positive dominant contribution to SEB at PR Col, compared to the K/H Divide and Kaskawulsh ELA, where longwave radiation dominates. At the lower two sites, the sensible heat flux also represents a small positive contribution during summer. In contrast, both the sensible and latent heat fluxes are



negative when calculated at PR Col. Wind speeds for turbulent flux heat calculations at PR Col were only available 24 July to 11 August 2021 (Fig. 8). However, July and August are during the height of the melt season, when we would expect turbulent  
260 fluxes to be the least negative (or most positive). We therefore expect the turbulent heat fluxes at PR Col to be predominately negative year-round.

## 4.2 Firn zones

Our results indicate that firn meltwater processes must be taken into account across both coastal and inland sectors of our AOI, and underscore the importance in developing robust meltwater percolation models for use in alpine environments; liquid  
265 water plays a central role in shaping near-surface physical properties across the majority of Wrangell/St. Elias. In fact, areas of dry firn are restricted to the highest peaks in the region, accounting for only 3% of our AOI. The limited extent of dry firn has direct implications for the preservation of paleoclimate archives, as meltwater percolation and refreezing in wet firn can disrupt stratigraphy and preclude drilling. As a result, opportunities to recover regional ice core records in Wrangell/St. Elias are already limited (Holland et al., 2026), and are likely to diminish with ongoing atmospheric warming.

270 We find elevations from approximately 3,000 m a.s.l. to 3,400 m a.s.l. to be a transitional zone between dry and wet firn conditions. High  $\Delta freeze$  values below this elevation indicate the persistence of liquid water within the firn into the fall, consistent with in situ observations of a firn aquifer near the Kaskawulsh/Hubbard Divide at approximately 2,640 m a.s.l. (Ochwat et al., 2021). Note that a delay in summer-to-winter backscatter rebound (high  $\Delta freeze$ ) does not necessarily imply a firn aquifer; a similar backscatter response can be expected from percolation and delayed refreeze even if an aquifer never  
275 forms.

We interpret this spatial transition zone as also reflecting a temporal transition: sites within this elevation band appear to be in the process of evolving from dry to increasingly wet firn states (e.g. increased percolation and delayed refreeze). This interpretation is supported by in situ observations and firn pack modeling at Eclipse Icefield (3,017 m a.s.l.) which suggest the site is undergoing a temporal transition from a mostly dry firn pack to one that can and does support persistent liquid water  
280 into the fall and winter (Kindstedt et al., 2025). If wetting of the firn continues to the point of saturation, this transition could support the eventual development of a firn aquifer. Even barring aquifer development, continued firn wetting will alter firn column structure and the timing of seasonal discharge from firn at these elevations.

We find elevations from approximately 1,000 m a.s.l. to 1,900 m a.s.l. to be a transitional zone between the wet firn and ablation zones. This is roughly consistent with locally estimated equilibrium line altitudes (“ELAs”; 1,750 m a.s.l. on the  
285 Nalüdäy Glacier and 2,100 m a.s.l. on the Kaskawulsh Glacier (Hill et al., 2021). The lower transition zone is less sharply defined than the upper, because the backscatter distinction between dry and wet snow/firn used in our freeze-up detection (with freeze-up in turn used to define transition zones) is obscured by the presence of other materials such as bare ice and debris.

The method applied here is able to identify the timing of seasonal melt onset and freeze-up; however, it does not provide information on other aspects of the melt season, such as intensity, total melt production, or the partitioning of meltwater between  
290 storage in the snow/firn column and runoff. Such factors are necessary to quantify the contribution of surface melt to glacier mass balance and assess downstream hydrological impacts. Notably, the variability in  $\Delta freeze$  between 3,000–3,400 m a.s.l.



suggests variation in melt season intensity, total melt production, and/or meltwater transport without a corresponding shift in melt onset, underscoring that onset alone is not a sufficient descriptor of seasonal melt dynamics. Nevertheless, in a region defined by pronounced seasonality, melt onset remains a valuable metric that establishes temporal context for subsequent melt, percolation, and refreezing processes. Future work should focus on the quantity and duration of meltwater retention in the firn, thereby enabling a more complete assessment of meltwater generation and its implications for both local glacier evolution and regional hydrology.

## 5 Conclusions

In this study, we present a spatially distributed assessment of seasonal surface melt onset and firn freeze-up across the Wrangell/St. Elias Mountains using satellite radar backscatter. By deriving melt timing metrics that are independent of air temperature, we provide the first region-wide characterization of surface melting and refreezing processes beyond the limits of in situ observations and temperature-based melt estimates. In particular, we show that surface melting can occur even where air temperatures remain below freezing year-round. Our results demonstrate the value of satellite SAR imagery for monitoring melt dynamics in complex, data-sparse mountain regions, while also highlighting the spatial variability of melt onset and the importance of local context when interpreting SAR signals.

We show that seasonal melt is widespread across the region, with wet firn, ablation zone, and transitional firn accounting for approximately 97% of the study area. Dry firn is confined to the highest elevations and represents only a small fraction of the landscape, substantially limiting the extent of firn capable of preserving undisturbed paleoclimate records. Seasonal backscatter evolution further indicates that meltwater persistence and delayed refreezing are common at mid-elevations, consistent with in situ observations and firn modeling that suggest increasingly water-rich firn conditions. Together, these findings highlight the central role of meltwater percolation and refreezing in shaping firn structure across much of Wrangell/St. Elias.

While the approach presented here is limited to resolving the timing of melt onset and freeze-up, these results provide a baseline for evaluating ongoing changes in glacier surface melt, alpine firn evolution, and downstream hydrological impacts in the Wrangell/St. Elias Mountains.

*Code and data availability.* Sentinel-1 SAR data can be downloaded through the Alaska Satellite Facility Vertex tool (<https://search.asf.alaska.edu/#/>). Glacier outlines are available online through the Global Land Ice Measurements from Space (GLIMS) initiative (<https://www.glims.org/RGI/>). The Mount Logan PR Col weather station data are available at: <https://www.hydrometcloud.com/MountLogan/>. The Kaskawulsh equilibrium line AWS data are available at: <https://datagarrison.com/users/300034012631040/300234068884730/plots.php>. HOBO and other AWS air temperature data are available on request from Dr. Luke Copland or Dr. Christine Dow. The base code used to produce these results is available on GitHub (<https://github.com/ac-johnson/GlacierSAR>).



## Appendix A: Sentinel-1 scenes used in this study

**Table A1.** Sentinel-1 scenes used in this study. *Total path/frames* and *Total scenes* are the total numbers of unique path/frames and scenes, respectively, over our area of interest each year. *Path/frames used* and *Scenes used* are the numbers of path/frames and scenes, respectively, used in our analysis after filtering. All scenes were obtained in the interferometric wide (IW) beam mode and in VV polarization.

Year	Total path/frames	Total scenes	Path/frames used	Scenes used
2015	22	125	4	61
2016	20	149	5	69
2017	12	239	6	161
2018	10	312	6	210
2019	10	318	6	212
2020	10	334	6	210
2021	10	330	6	204
2022	10	198	4	138
2023	6	166	4	136
2024	8	180	4	128



## Appendix B: Isotherm computation from in situ temperature data

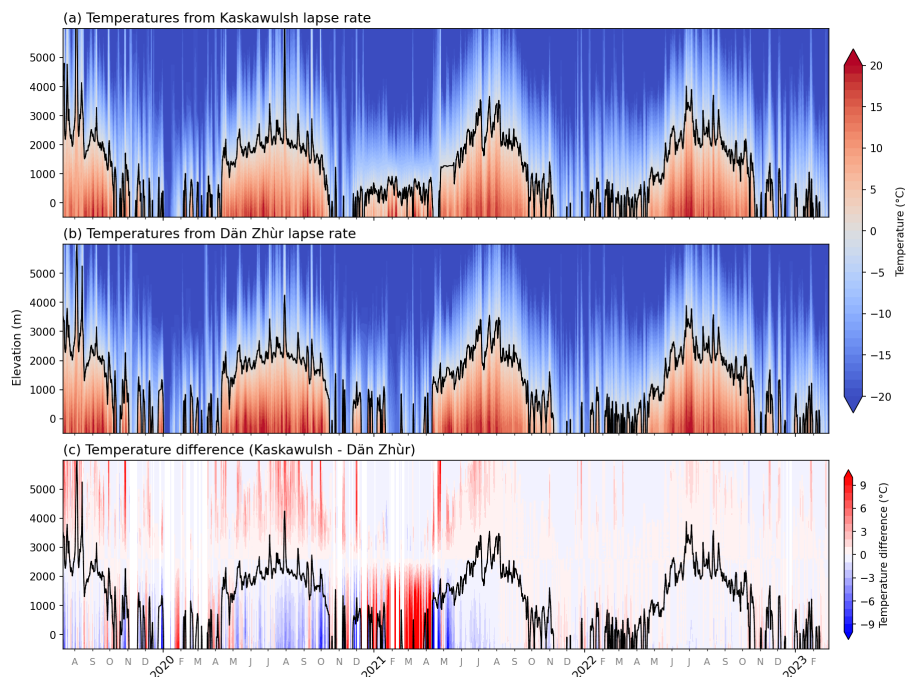


**Figure B1.** Isotherms computed from Kaskawulsh vs. Dän Zhùr air temperature data over their period of overlap (July 2019 – February 2023). In situ data were used to calculate lapse rates, which were in turn used to estimate temperatures by elevation. Panel (a) shows temperature estimates based on in situ measurements from the Kaskawulsh Glacier. Panel (b) shows temperature measurements based on in situ data from the Dän Zhùr Glacier. Panel (c) shows the difference between the two. Station locations shown in Figure 1, and station information in Table 1.



### Appendix C: Definition of firn zones

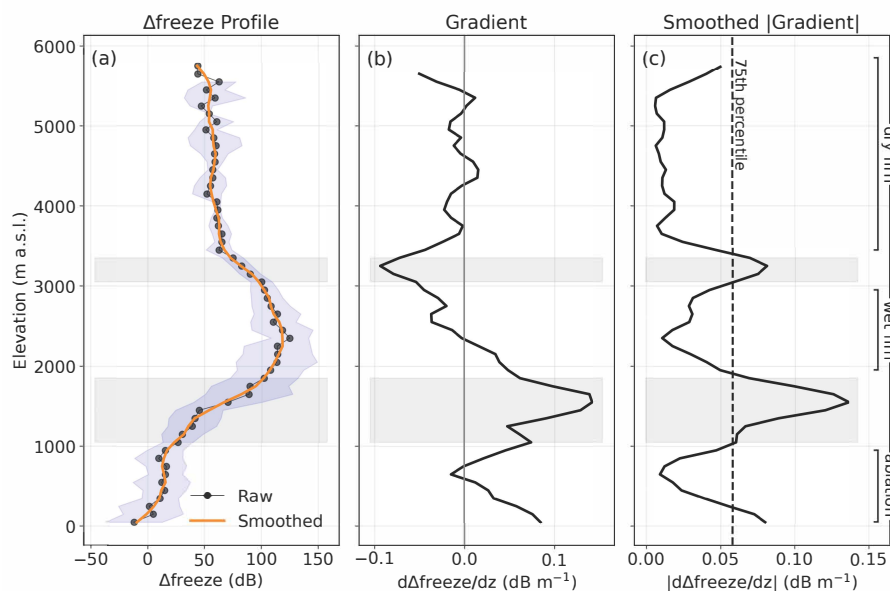


**Figure C1.**  $\Delta freeze$  profile (a), vertical gradient (b), and vertical gradient absolute value (c) used to define firn zones. Mean unsmoothed  $\Delta freeze$  in panel (a) are shown by black circles with the standard deviation shown by the shaded blue envelope; the smoothed curve is shown by the solid orange line. Smoothing is done using a Savitzky–Golay filter; where insufficient data density preclude Savitzky–Golay filtering, a centered rolling mean is applied. The vertical gray line in panel (b) indicated a vertical  $\Delta freeze$  gradient of zero. The vertical dashed line in panel (c) indicates the 75th percentile of  $\Delta freeze$  vertical gradient absolute values. Transitional firn zones are shown by the horizontal shaded gray bars.



### Appendix D: Melt onset and freeze-up maps for individual years

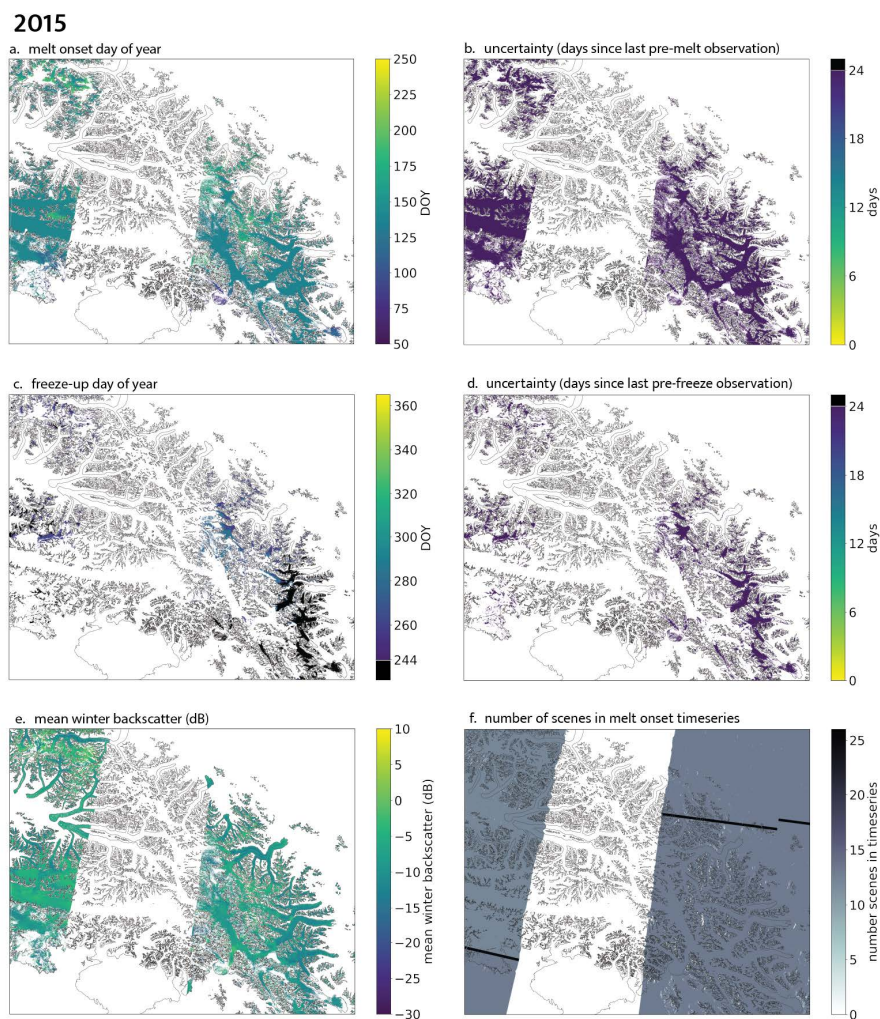


**Figure D1.** Melt onset (a), onset uncertainty (b), freeze-up (c), freeze-up uncertainty (d), mean winter backscatter (e), and number of scenes (f) over our area of interest (AOI) for 2015.

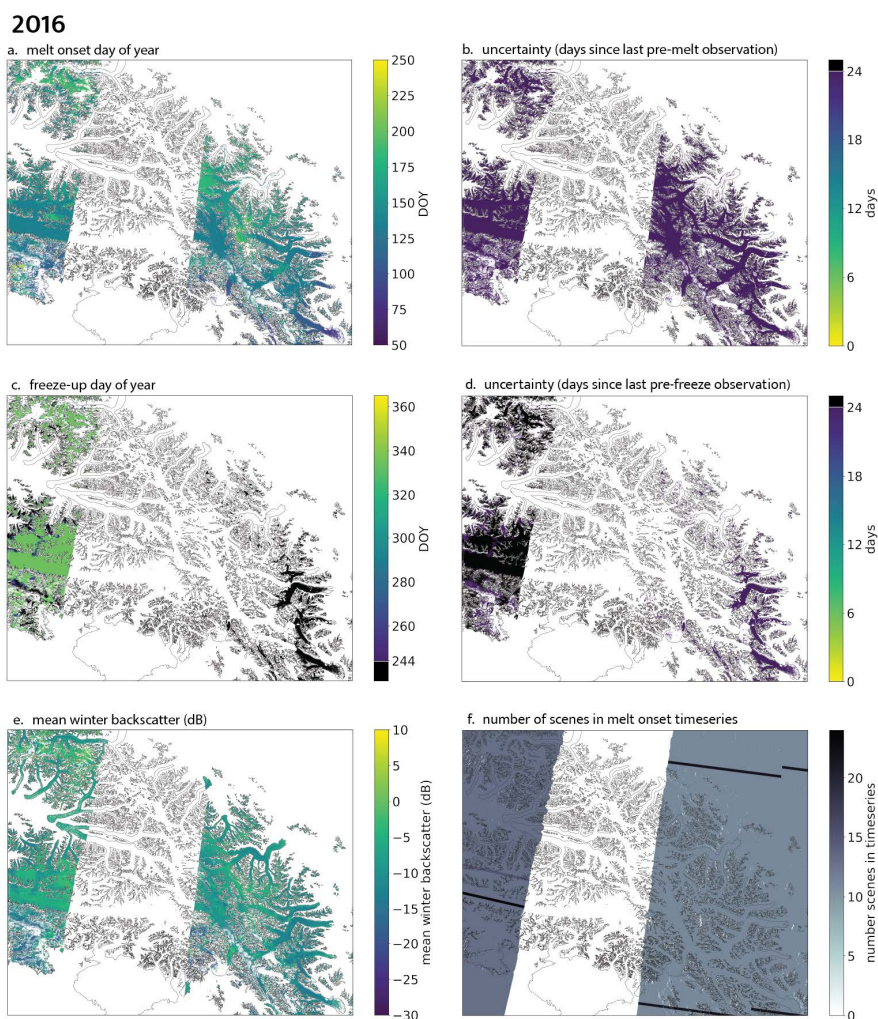


**Figure D2.** Melt onset (a), onset uncertainty (b), freeze-up (c), freeze-up uncertainty (d), mean winter backscatter (e), and number of scenes (f) over our area of interest (AOI) for 2016.

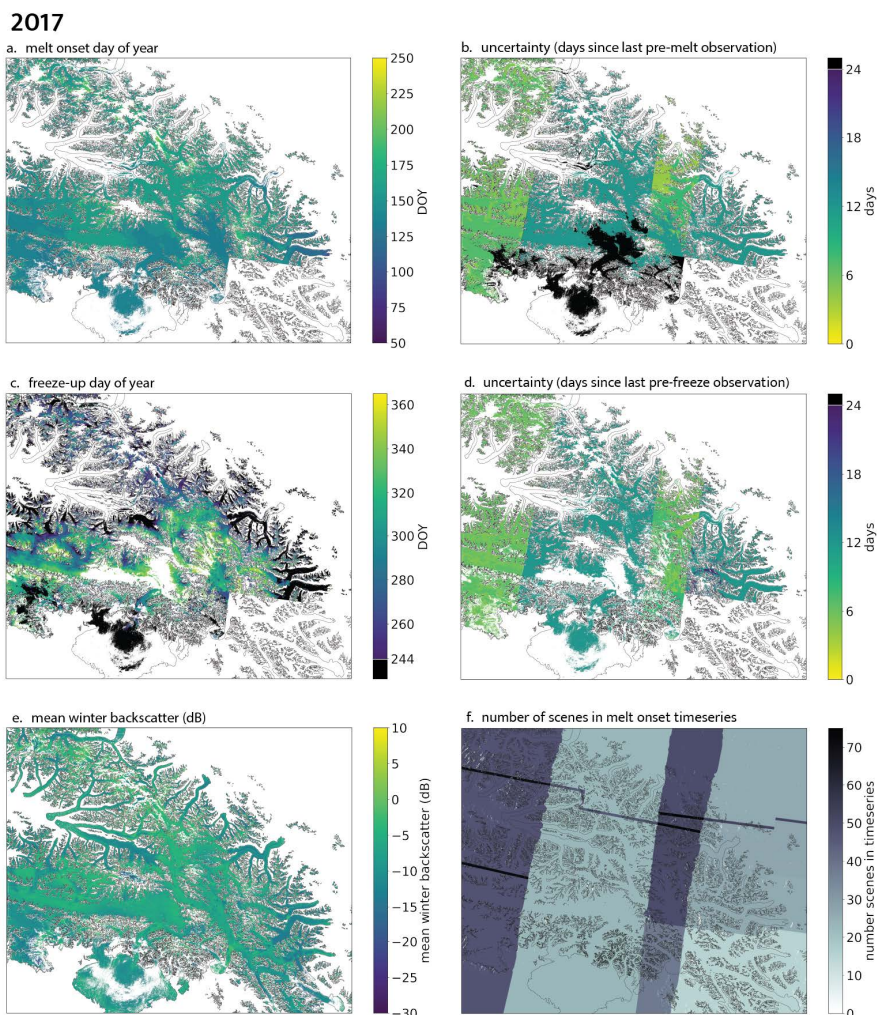


**Figure D3.** Melt onset (a), onset uncertainty (b), freeze-up (c), freeze-up uncertainty (d), mean winter backscatter (e), and number of scenes (f) over our area of interest (AOI) for 2017.



2018

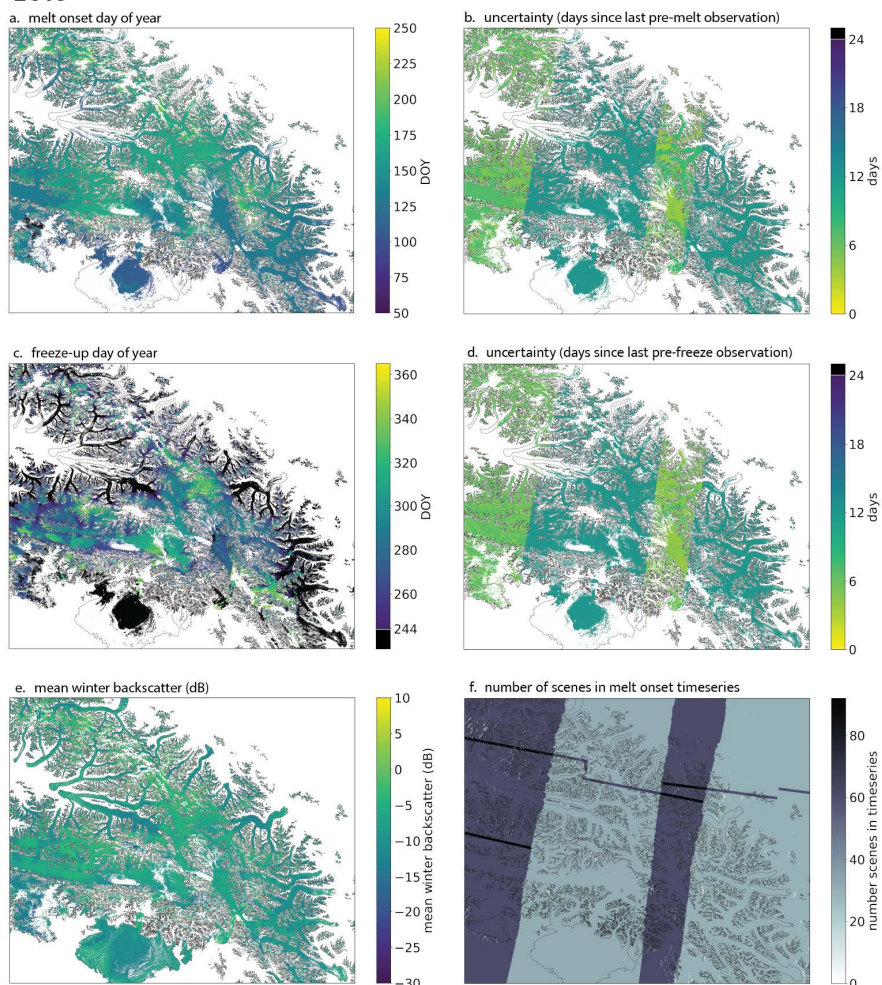


**Figure D4.** Melt onset (a), onset uncertainty (b), freeze-up (c), freeze-up uncertainty (d), mean winter backscatter (e), and number of scenes (f) over our area of interest (AOI) for 2018.

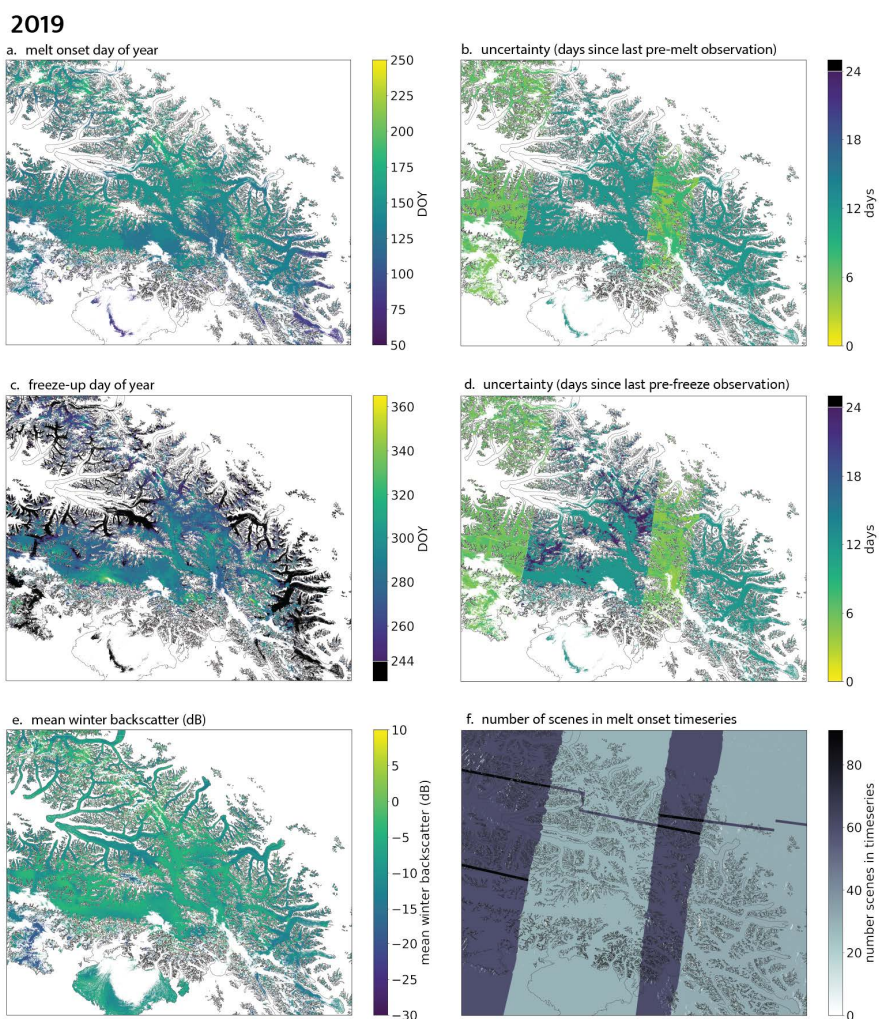


**Figure D5.** Melt onset (a), onset uncertainty (b), freeze-up (c), freeze-up uncertainty (d), mean winter backscatter (e), and number of scenes (f) over our area of interest (AOI) for 2019.

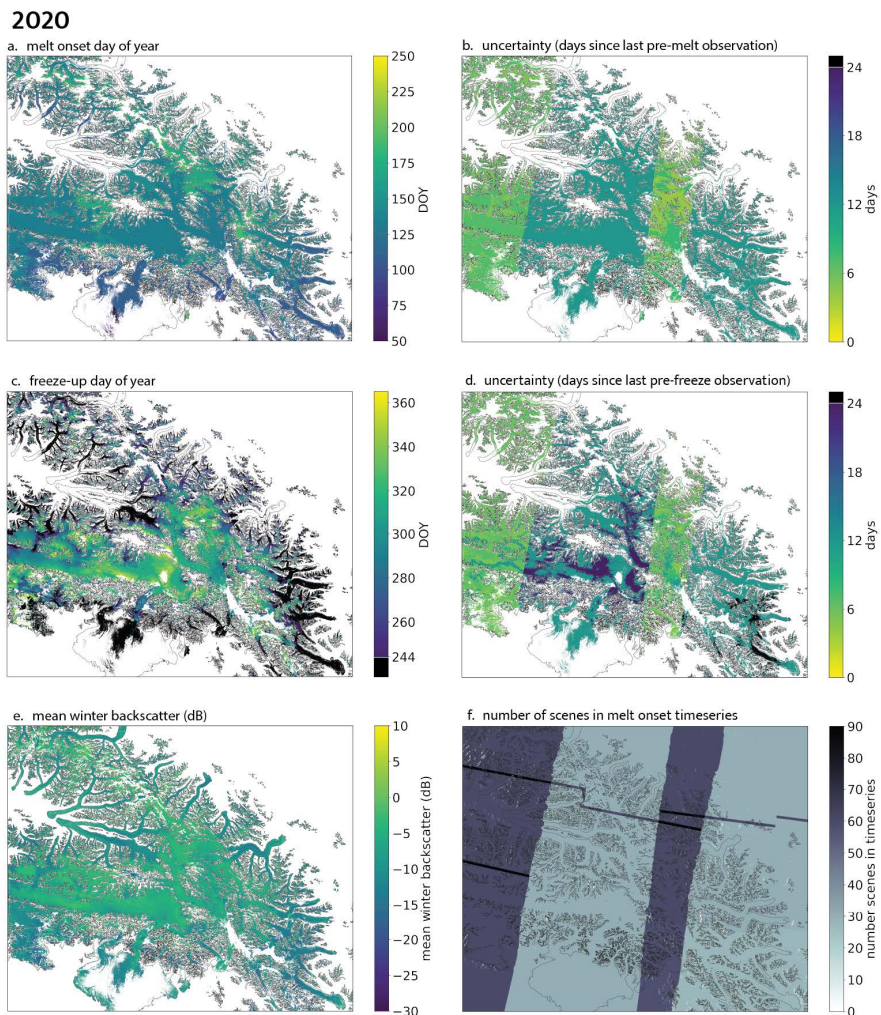


**Figure D6.** Melt onset (a), onset uncertainty (b), freeze-up (c), freeze-up uncertainty (d), mean winter backscatter (e), and number of scenes (f) over our area of interest (AOI) for 2020.

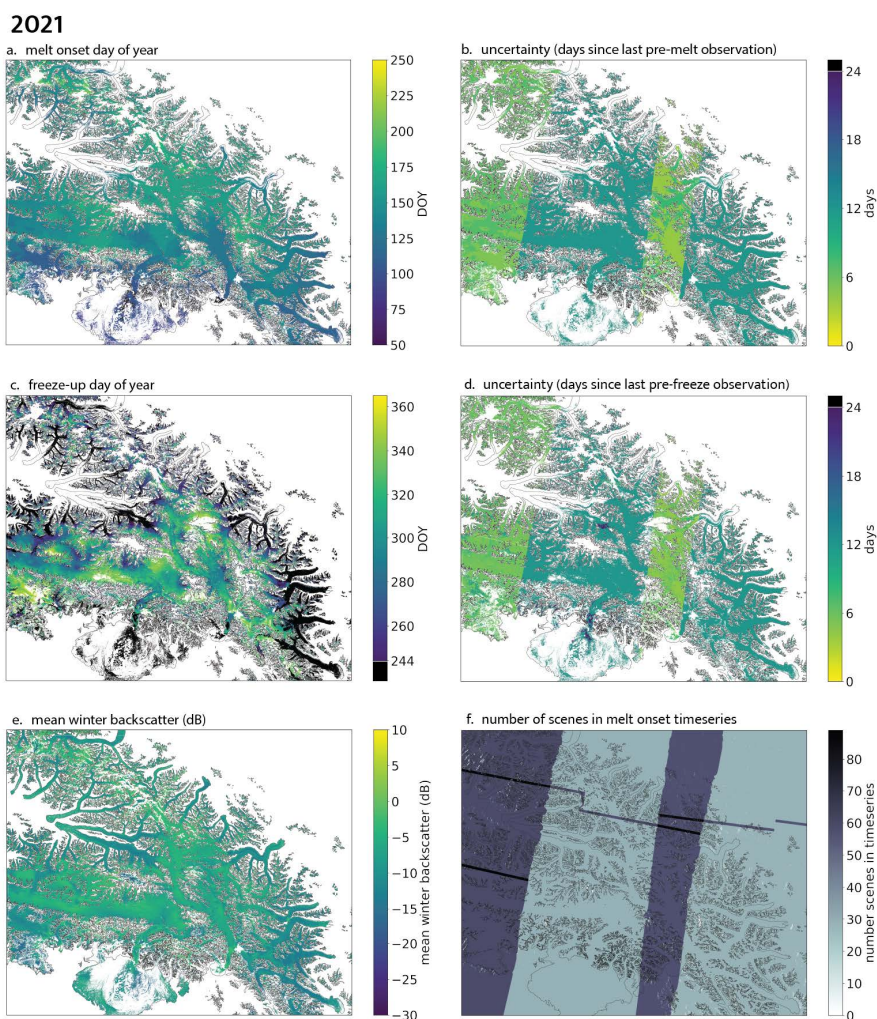


**Figure D7.** Melt onset (a), onset uncertainty (b), freeze-up (c), freeze-up uncertainty (d), mean winter backscatter (e), and number of scenes (f) over our area of interest (AOI) for 2021.

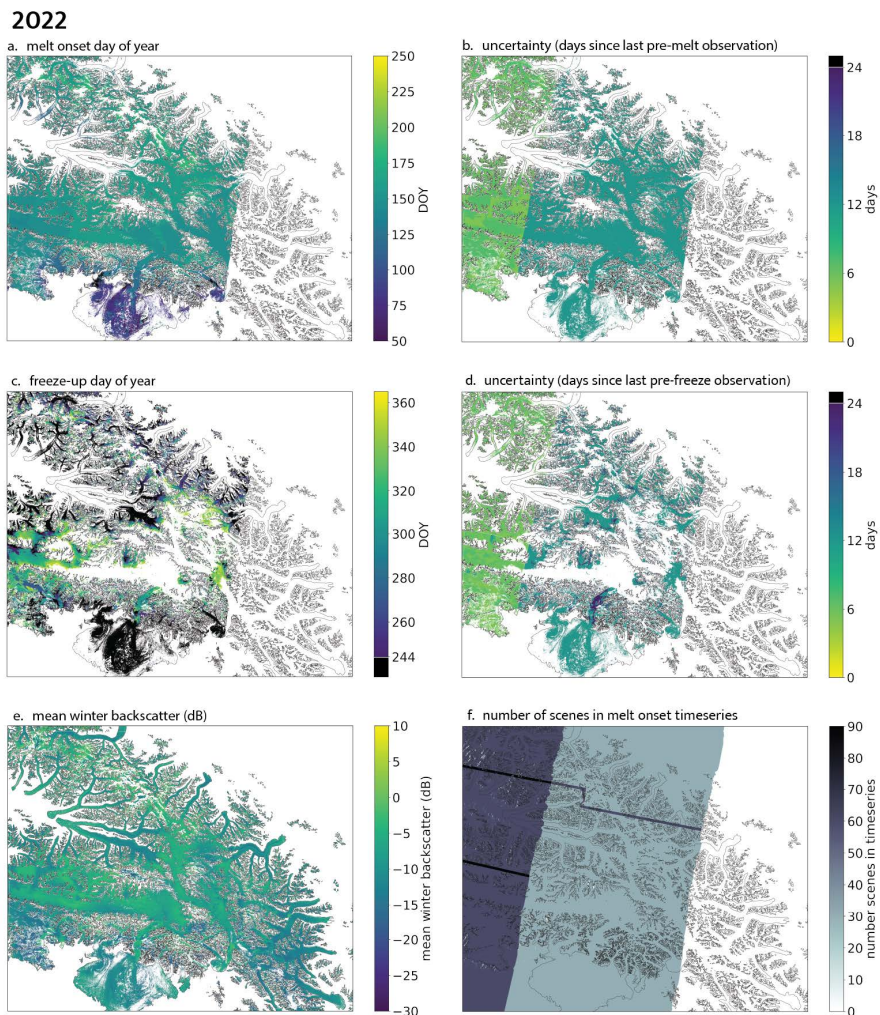


**Figure D8.** Melt onset (a), onset uncertainty (b), freeze-up (c), freeze-up uncertainty (d), mean winter backscatter (e), and number of scenes (f) over our area of interest (AOI) for 2022.



2023

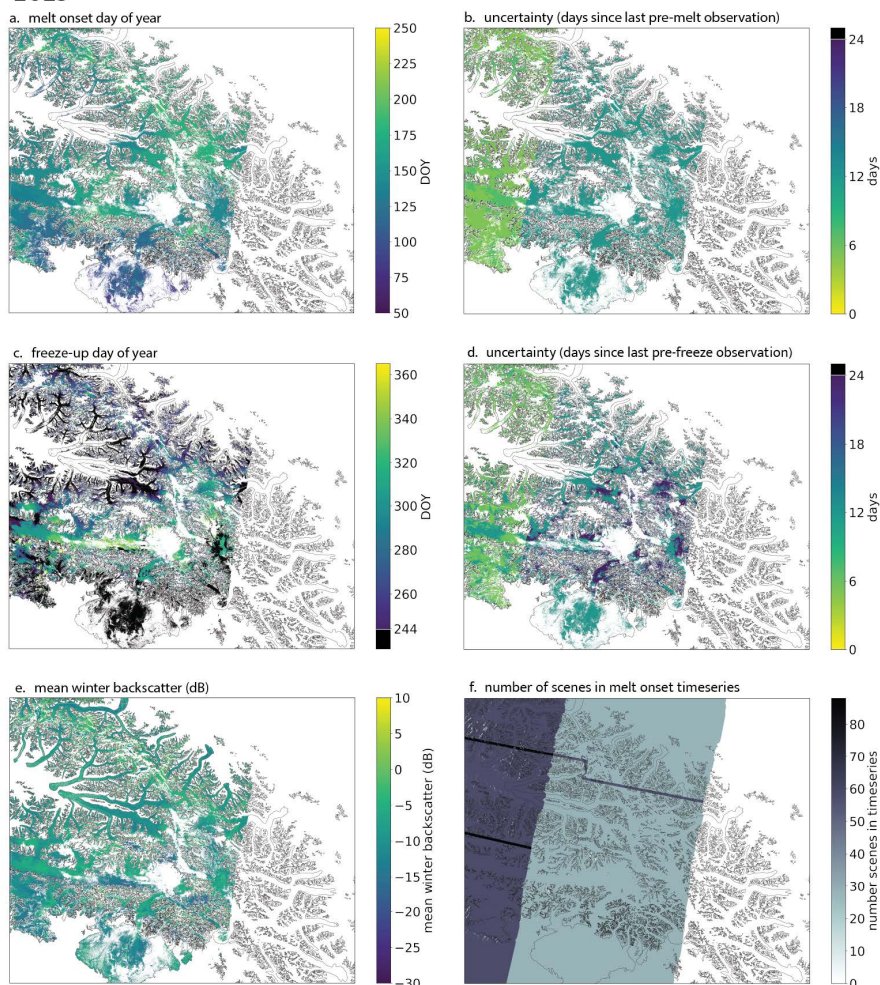


**Figure D9.** Melt onset (a), onset uncertainty (b), freeze-up (c), freeze-up uncertainty (d), mean winter backscatter (e), and number of scenes (f) over our area of interest (AOI) for 2023.



2024

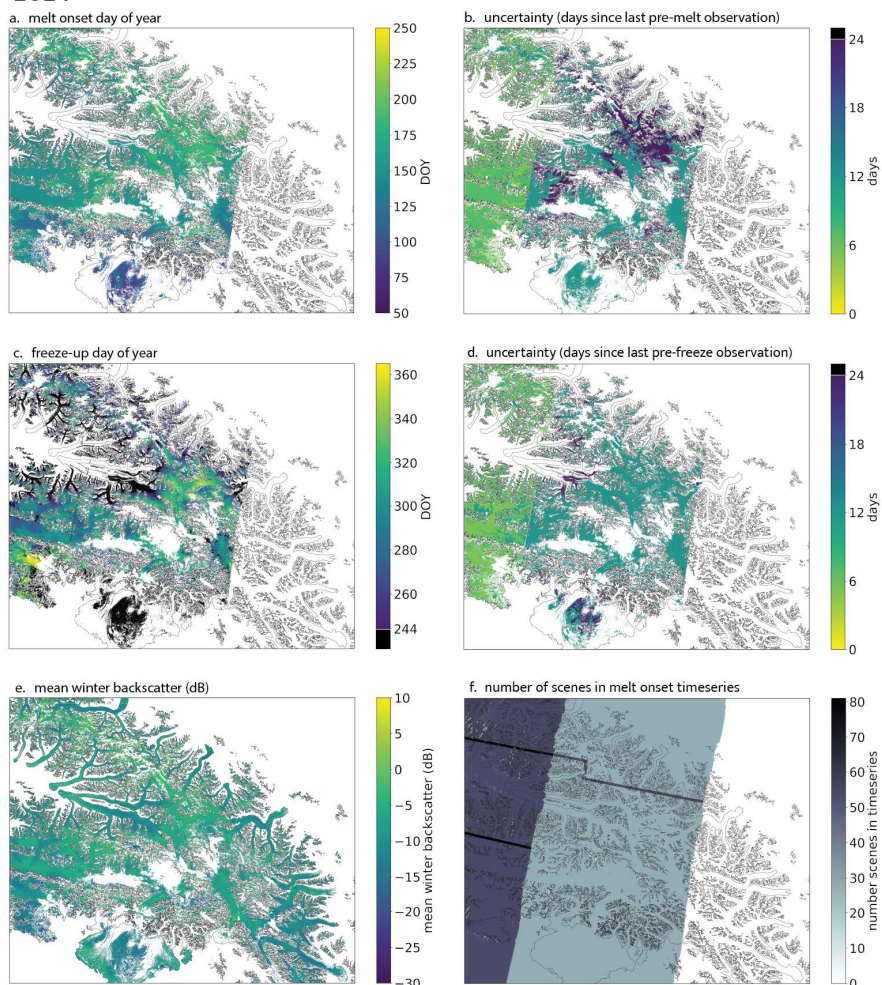


**Figure D10.** Melt onset (a), onset uncertainty (b), freeze-up (c), freeze-up uncertainty (d), mean winter backscatter (e), and number of scenes (f) over our area of interest (AOI) for 2024.



325 *Author contributions.* IK, KS, KK, DW, LC, and SC formulated the research goals, hypotheses and testing methods. LC, CD, and AC provided in situ weather data. AJ wrote the base code used by IK in data analysis. IK completed analysis with contributions from KS, AJ, LC, KK, DW, and SC. IK prepared the manuscript with contributions from all co-authors.

*Competing interests.* The contact author has declared that none of the authors has any competing interests.

330 *Acknowledgements.* We thank the Kluane, Champagne and Aishihik, and White River First Nations, on whose traditional territories our snow sounders were deployed. We thank Kluane National Park and Reserve (Parks Canada), Icefield Discovery, Kluane Lake Research Station and the Arctic Institute of North America for collaboration and support. Funding provided by the Natural Sciences and Engineering Research Council of Canada (NSERC RGPIN-2025-03982), Canada Foundation for Innovation, University of Ottawa, Polar Continental Shelf Program, the Canada Research Chairs Program, and ArcticNet, through the Strategic Science Fund. Support to ASC from the National Geographic Society funded the installation of the Mount Logan PR Col weather station.



### 335 References

- Baghdadi, N., Gauthier, Y., and Bernier, M.: Capability of multitemporal ERS-1 SAR data for wet-snow mapping, *Remote Sensing of Environment*, 60, 174–186, [https://doi.org/10.1016/S0034-4257\(96\)00180-0](https://doi.org/10.1016/S0034-4257(96)00180-0), 1997.
- Bezeau, P., Sharp, M., Burgess, D., and Gascon, G.: Firn profile changes in response to extreme 21st-century melting at Devon Ice Cap, Nunavut, Canada, *Journal of Glaciology*, 59, 981–991, <https://doi.org/10.3189/2013JOG12J208>, publisher: Cambridge University Press, 340 2013.
- Brutsaert, W.: On a derivable formula for long-wave radiation from clear skies, *Water Resources Research*, 11, 742–744, <https://doi.org/https://doi.org/10.1029/WR011i005p00742>, 1975.
- Cuffey, K. M. and Paterson, W. S. B.: *The Physics of Glaciers*, Elsevier, 4th edn., 2010.
- Culberg, R., Schroeder, D. M., and Chu, W.: Extreme melt season ice layers reduce firn permeability across Greenland, *Nature Communications* 2021 12:1, 12, 1–9, <https://doi.org/10.1038/S41467-021-22656-5>, publisher: Nature Publishing Group, 2021. 345
- European Space Agency (ESA): Digital Elevation Model, <https://doi.org/10.5270/ESA-c5d3d65>, 2014.
- Fountain, A. G.: The Storage of Water in, and Hydraulic Characteristics of, the Firn of South Cascade Glacier, Washington State, U.S.A., *Annals of Glaciology*, 13, 69–75, <https://doi.org/10.3189/S0260305500007667>, publisher: Cambridge University Press, 1989.
- Harper, J., Humphrey, N., Pfeffer, W. T., Brown, J., and Fettweis, X.: Greenland ice-sheet contribution to sea-level rise buffered by meltwater storage in firn, *Nature* 2012 491:7423, 491, 240–243, <https://doi.org/10.1038/NATURE11566>, publisher: Nature Publishing Group, 2012. 350
- Hill, T., Dow, C. F., Bash, E. A., and Copland, L.: Application of an improved surface energy balance model to two large valley glaciers in the St. Elias Mountains, Yukon, *Journal of Glaciology*, 67, 297–312, <https://doi.org/10.1017/JOG.2020.106>, publisher: Cambridge University Press, 2021.
- Hock, R.: Temperature index melt modelling in mountain areas, *Journal of Hydrology*, 282, 104–115, [https://doi.org/https://doi.org/10.1016/S0022-1694\(03\)00257-9](https://doi.org/https://doi.org/10.1016/S0022-1694(03)00257-9), *mountain Hydrology and Water Resources*, 2003. 355
- Hock, R.: Glacier melt: a review of processes and their modelling, *Progress in Physical Geography: Earth and Environment*, 29, 362–391, <https://doi.org/10.1191/0309133305pp453ra>, publisher: SAGE Publications Ltd, 2005.
- Hogenson, K., Kristenson, H., Kennedy, J., Johnson, A., Rine, J., Logan, T., Zhu, J., Williams, F., Hermann, J., Smale, J., and Meyer, F.: Hybrid Pluggable Processing Pipeline (HyP3): A cloud-native infrastructure for generic processing of SAR data., 2020.
- Holland, K. M., Criscitiello, A. S., McConnell, J. R., Markle, B. R., Yousif, H. A. K., Skelton, E., Wensman, S. M., Jensen, B. J. L., Winski, D. A., Campbell, S. W., and Chellman, N. J.: Unexpectedly High Accumulation Rates in the 2022 Mt. Logan Ice Core Reveal Warm-Season Drivers of Precipitation Variability, *Journal of Geophysical Research: Atmospheres*, 131, e2025JD044951, <https://doi.org/https://doi.org/10.1029/2025JD044951>, e2025JD044951 2025JD044951, 2026. 360
- Horlings, A. N., Christianson, K., and Miège, C.: Expansion of Firn Aquifers in Southeast Greenland, *Journal of Geophysical Research: Earth Surface*, 127, e2022JF006753, <https://doi.org/10.1029/2022JF006753>, publisher: John Wiley & Sons, Ltd, 2022. 365
- Jansson, P., Hock, R., and Schneider, T.: The concept of glacier storage: a review, *Journal of Hydrology*, 282, 116–129, [https://doi.org/10.1016/S0022-1694\(03\)00258-0](https://doi.org/10.1016/S0022-1694(03)00258-0), publisher: Elsevier, 2003.
- Johnson, A.: GlacierSAR, <https://github.com/ac-johnson/GlacierSAR?tab=readme-ov-file#glaciersar>, 2023.
- Kindstedt, I., Winski, D., Stevens, C. M., Skelton, E., Copland, L., Kreutz, K., Mannello, M., Clavette, R., Holmes, J., Albert, M., and Williamson, S. N.: Ongoing firn warming at Eclipse Icefield, Yukon, indicates potential widespread meltwater percolation and retention in firn pack across the St. Elias Range, *The Cryosphere*, 2025, 1–39, <https://doi.org/10.5194/egusphere-2024-3807>, 2025. 370



- Kindstedt, I., Winski, D., Copland, L., Loso, M., Kreutz, K., and Zdanowicz, C.: Air trajectories and snowfall over Alaska-Yukon icefields: Implications for ice-core accumulation studies, *Journal of Glaciology*, p. 1–24, <https://doi.org/10.1017/jog.2026.10142>, 2026.
- 375 Koenig, L. S., Miège, C., Forster, R. R., and Brucker, L.: Initial in situ measurements of perennial meltwater storage in the Greenland firn aquifer, *Geophysical Research Letters*, 41, 81–85, <https://doi.org/10.1002/2013GL058083>, publisher: John Wiley & Sons, Ltd, 2014.
- Lievens, H., Demuzere, M., Marshall, H. P., Reichle, R. H., Brucker, L., Brangers, I., de Rosnay, P., Dumont, M., Giroto, M., Immerzeel, W. W., Jonas, T., Kim, E. J., Koch, I., Marty, C., Saloranta, T., Schöber, J., and Lannoy, G. J. D.: Snow depth variability in the Northern Hemisphere mountains observed from space, *Nature Communications* 2019 10:1, 10, 1–12, <https://doi.org/10.1038/S41467-019-12566-Y>, 2019.
- 380 MacFerrin, M., Machguth, H., As, D. v., Charalampidis, C., Stevens, C. M., Heilig, A., Vandecrux, B., Langen, P. L., Mottram, R., Fettweis, X., Broeke, M. R. v. d., Pfeffer, W. T., Moussavi, M. S., and Abdalati, W.: Rapid expansion of Greenland’s low-permeability ice slabs, *Nature* 2019 573:7774, 573, 403–407, <https://doi.org/10.1038/S41586-019-1550-3>, publisher: Nature Publishing Group, 2019.
- Machguth, H., Macferrin, M., As, D. V., Box, J. E., Charalampidis, C., Colgan, W., Fausto, R. S., Meijer, H. A. J., Mosley-Thompson, E., and Wal, R. S. W. V. D.: Greenland meltwater storage in firn limited by near-surface ice formation, *Nature Climate Change* 2016 6:4, 6, 390–393, <https://doi.org/10.1038/NCLIMATE2899>, publisher: Nature Publishing Group, 2016.
- 385 Marcus, M. G. and Ragle, R. H.: Snow Accumulation in the Icefield Ranges, St. Elias Mountains, Yukon, *Arctic and Alpine Research*, 2, 277–292, <https://doi.org/10.1080/00040851.1970.12003587>, publisher: Taylor & Francis, 1970.
- Matthews, T., Perry, L. B., Koch, I., Aryal, D., Khadka, A., Shrestha, D., Abernathy, K., Elmore, A. C., Seimon, A., Tait, A., Elvin, S., Tuladhar, S., Baidya, S. K., Potocki, M., Birkel, S. D., Kang, S., Sherpa, T. C., Gajurel, A., and Mayewski, P. A.: Going to Extremes: 390 Installing the World’s Highest Weather Stations on Mount Everest, *Bulletin of the American Meteorological Society*, 101, E1870–E1890, <https://doi.org/10.1175/BAMS-D-19-0198.1>, 2020.
- Miller, M. M.: The terms “Névé” and “Firn”, *Journal of Glaciology*, 2, 150–151, <https://doi.org/10.3189/S0022143000034195>, publisher: Cambridge University Press, 1952.
- Miège, C., Forster, R. R., Brucker, L., Koenig, L. S., Solomon, D. K., Paden, J. D., Box, J. E., Burgess, E. W., Miller, J. Z., McNerney, 395 L., Brautigam, N., Fausto, R. S., and Gogineni, S.: Spatial extent and temporal variability of Greenland firn aquifers detected by ground and airborne radars, *Journal of Geophysical Research: Earth Surface*, 121, 2381–2398, <https://doi.org/10.1002/2016JF003869>, iSBN: 10.1002/2016 Publisher: John Wiley & Sons, Ltd, 2016.
- Nagler, T. and Rott, H.: Retrieval of wet snow by means of multitemporal SAR data, *IEEE Transactions on Geoscience and Remote Sensing*, 38, 754–765, <https://doi.org/10.1109/36.842004>, 2000.
- 400 Nagler, T., Rott, H., Ripper, E., Bippus, G., and Hetzenecker, M.: Advancements for Snowmelt Monitoring by Means of Sentinel-1 SAR, *Remote Sensing* 2016, Vol. 8, Page 348, 8, 348, <https://doi.org/10.3390/RS8040348>, 2016.
- Newman, A. J., Clark, M. P., Wood, A. W., and Arnold, J. R.: Probabilistic Spatial Meteorological Estimates for Alaska and the Yukon, *Journal of Geophysical Research: Atmospheres*, 125, <https://doi.org/10.1029/2020JD032696>, 2020.
- Ochwat, N. E., Marshall, S. J., Moorman, B. J., Criscitiello, A. S., and Copland, L.: Evolution of the firn pack of Kaskawulsh Glacier, Yukon: 405 Meltwater effects, densification, and the development of a perennial firn aquifer, *Cryosphere*, 15, 2021–2040, <https://doi.org/10.5194/TC-15-2021-2021>, publisher: Copernicus GmbH, 2021.
- Polashenski, C., Courville, Z., Benson, C., Wagner, A., Chen, J., Wong, G., Hawley, R., and Hall, D.: Observations of pronounced Greenland ice sheet firn warming and implications for runoff production, *Geophysical Research Letters*, 41, 4238–4246, <https://doi.org/10.1002/2014GL059806>, publisher: John Wiley & Sons, Ltd, 2014.



- 410 Rau, F., Braun, M., Friedrich, M., Weber, F., and Goßmann, H.: Radar glacier zones and their boundaries as indicators of glacier mass balance and climatic variability, in: Proceedings of EARSeL-SIG-Workshop Land Ice and Snow, BINDSCHADLER, 2000.
- RGI 7.0 Consortium, R. . . : Randolph Glacier Inventory - A Dataset of Global Glacier Outlines, Version 7.0, 2023.
- Samimi, S. and Marshall, S. J.: Diurnal cycles of meltwater percolation, refreezing, and drainage in the supraglacial snowpack of Haig Glacier, Canadian Rocky Mountains, *Frontiers in Earth Science*, 5, 6, <https://doi.org/10.3389/FEART.2017.00006/BIBTEX>, publisher: Frontiers Media S.A., 2017.
- 415 Scher, C., Steiner, N. C., and McDonald, K. C.: Mapping seasonal glacier melt across the Hindu Kush Himalaya with time series synthetic aperture radar (SAR), *Cryosphere*, 15, 4465–4482, <https://doi.org/10.5194/TC-15-4465-2021>, 2021.
- Schneider, T.: Water movement in the firn of Storglaciären, Sweden, *Journal of Glaciology*, 45, 286–294, <https://doi.org/10.3189/S0022143000001787>, publisher: Cambridge University Press, 1999.
- 420 Sergeant, C. J., Falke, J. A., Bellmore, R. A., Bellmore, J. R., and Crumley, R. L.: A Classification of Streamflow Patterns Across the Coastal Gulf of Alaska, *Water Resources Research*, 56, e2019WR026 127, <https://doi.org/10.1029/2019WR026127>, 2020.
- Shi, J. and Dozier, J.: Inferring Snow Wetness Using C-Band Data from SIR-C’s Polarimetric Synthetic Aperture Radar, *IEEE Transactions on Geoscience and Remote Sensing*, 33, 905–914, <https://doi.org/10.1109/36.406676>, 1995.
- Tsai, Y.-L. S., Dietz, A., Oppelt, N., and Kuenzer, C.: Remote Sensing of Snow Cover Using Spaceborne SAR: A Review, *Remote Sensing*, 11, 1456, <https://doi.org/10.3390/rs11121456>, number: 12 Publisher: Multidisciplinary Digital Publishing Institute, 2019.
- 425 Vandecrux, B., Fausto, R. S., van As, D., Colgan, W., Langen, P. L., Haubner, K., Ingeman-Nielsen, T., Heilig, A., Stevens, C. M., MacFerrin, M., and et al.: Firn cold content evolution at nine sites on the Greenland ice sheet between 1998 and 2017, *Journal of Glaciology*, 66, 591–602, <https://doi.org/10.1017/jog.2020.30>, 2020.
- Williamson, S. N., Zdanowicz, C., Anslow, F. S., Clarke, G. K. C., Copland, L., Danby, R. K., Flowers, G. E., Holdsworth, G., Jarosch, A. H., and Hik, D. S.: Evidence for elevation-dependent warming in the St. Elias Mountains, Yukon, Canada, *Journal of Climate*, 33, 3253–3269, <https://doi.org/10.1175/JCLI-D-19-0405.1>, 2020.
- 430 Winsvold, S. H., Kääb, A., Nuth, C., Andreassen, L. M., Pelt, W. J. V., and Schellenberger, T.: Using SAR satellite data time series for regional glacier mapping, *Cryosphere*, 12, 867–890, <https://doi.org/10.5194/TC-12-867-2018>, 2018.